Degradation of alkali-activated Fe-rich slag in magnesium sulfate solution

Nana Wen[a*], Vincent Hallet[a], Arne Peys[b], Yiannis Pontikes[a]

[a] KU Leuven Department of Materials Engineering, Kasteelpark Arenberg 44, 3001 Leuven, Belgium
[b] Sustainable Materials Management, VITO, Boeretang 200, 2400, Mol, Belgium

*Correspondent author: Nana Wen, nana.wen@kuleuven.be

Highlights

Alkali-activated Fe-rich slag shows good resistance to $MgSO_4$ attack.

Unreacted slag is inert to $MgSO_4$ attack.

Increase of Mg content in the slag leads to higher corrosion depth.

Moderate Ca/Si in the slag showed the highest strength retention.

Formation of $Mg(OH)_2$ after $MgSO_4$ attack highly protects the matrix.

Abstract

The potential of Fe-rich non-ferrous metallurgical slag (NFMS) in alkali-activated materials has been demonstrated, exhibiting promising mechanical strength and fire resistance. However, the durability of alkali-activated NFMS (AA-NFMS) in terms of sulfate salt resistance remains unexplored. Additionally, the variability in the chemical composition of NFMS presents challenges in directly assessing the durability of AA-NFMS. This study investigates the interplay between the Ca/Si and Mg/Ca ratios in Fe-rich NFMS and the resulting $MgSO_4$ resistance of the AA-NFMS made thereof. To do so, mass change and retention in compressive strength were monitored for six months on AA-NFMS immersed in 5 wt.% $MgSO_4$, whereas microstructure was investigated using scanning electron microscope (SEM) and electron probe microanalyzer (EPMA). The results show that the $MgSO_4$ solution attacked selectively the reacted binder matrix of AA-NFMS rather than the unreacted slag. The

corrosion primarily occurs at the sulfate exposure surface of AA-NFMS, forming a dense, thin layer of $Mg(OH)_2$, which acts as a barrier and impedes further attack. Dissolution of Ca is the most pronounced among the major elements (Ca, Fe, Al, and Si) in the NFMS. The mass of the specimens increased linearly with the initial Ca content. The medium Ca concentration (~10%) retained the highest strength.

Keywords

Fe-rich slag, alkali-activated material, slag chemistry, $MgSO_4$ resistance

Introduction

Climate change and the contribution of cement production to the above has intensified the need for sustainable alternative binders [1]. Alkali-activated materials (AAM) are one of the most promising eco-friendly alternatives [2]. AAM are typically produced from ground granulated blast furnace slag (GGBFS) and fly ash precursors. Still, these materials are already used in blended cements, whereas the decarbonization efforts in both iron metallurgy and energy production lead to lower available quantities of GGBFS and fly ash, respectively [3]. To address these issues, new precursors such as Fe-rich non-ferrous metallurgical slag (NFMS), which are generated from Cu, Pb, Co/Ni, or Sn metallurgical industry, have been investigated [4]. This approach not only tackles the aforementioned issues, but also contributes to sustainability by utilizing residual materials.

Most existing studies only pay attention to the process of alkali activation and mechanical performance [5], with few addressing the fire resistance of alkali-activated NFMS (AA-NFMS) [6], leading to a knowledge gap regarding various durability aspects. After corrosion of the reinforcement, sulfate attack is the second major durability problem, causing damage to concrete structures already after a short period (10-15 years) [7, 8]. Sulfate ions in soils, underground water, industrial effluents and seawater could potentially cause the deterioration of cement-based materials. The SO_4^{2-} reacts with the monosulfate, calcium aluminates, portlandite, and C-S-H gel in the cement, leading to the formation of gypsum, ettringite, or thaumasite [9-12]. These phases generate expansion and internal stress when

formed at a late age, causing subsequent cracking and weakening of the concrete structure [13]. The most common sulfate salts are $CaSO_4$, Na_2SO_4, K_2SO_4, $(NH_4)_2SO_4$ and $MgSO_4$. Among these sulfate salts, $MgSO_4$ is found to be the most aggressive [14, 15]. Apart from the reaction of sulfate ions, Mg^{2+} can replace Ca^{2+} in the hydrated cement phases resulting in the formation of brucite and magnesium silicate hydrates [16]. The replaced Ca precipitates mainly as gypsum [17].

While AAM are often touted as having high sulfate resistance, in some cases, sulfate attack has led to expansion in the structure and reduced strength [18, 19]. For example, alkali-activated GGBFS (AA-GGBFS) has been observed to experience a 34% reduction in compressive strength and 0.021% increase in length after exposure to $MgSO_4$ solution for 365 days [20]. Ye et al. [21] reported that upon $MgSO_4$ attack, the original reaction product C-A-S-H is turned into gypsum and M-A-S-H, due to the decalcification of C-A-S-H and the intrusion of Mg^{2+} and SO_4^{2-}. A dense layer of brucite might sometimes form depending on the pH of the pore solution, protecting it from further corrosion.

AA-NFMS is a Fe-silicate binder that differs in reaction products from traditional aluminosilicate binders (such as F-class fly ash or metakaolin) and calcium aluminosilicate binders (such as GGBFS) commonly used in AAM. As a relatively new precursor for AAM, there is a growing need to understand the $MgSO_4$ resistance of AA-NFMS comprehensively. It is previously reported [22] that the extent of the structural changes of AAM in a sulfate-rich environment is highly affected by the chemistry of the precursor. The composition of NFMS can vary regionally and as a function of time due to its by-product/residue status. Generally, NFMS consists of FeO (around 20-60 wt.%) and SiO_2 (22-35 wt.%) as the primary chemical components, with minor amounts of Al_2O_3 (2-13%) and CaO (0.5-20%) [6]. In certain instances, industrial NFMS may also contain small amounts of MgO (0-11 wt.%). The CaO content was found to play a crucial role in the mechanical performance of AA-NFMS [23-26]. While the influence of Ca concentration on the mechanical strength of AA-NFMS has been extensively studied [23-26], its effect on $MgSO_4$ resistance remains unclear. Moreover, the impact of Mg on AA-NFMS has not yet been explored. The study of the effects of Mg in AA-NFMS is essential to broaden our understanding and identify potential opportunities for developing more sustainable and durable construction materials.

In this context, we investigate the $MgSO_4$ resistance of AA-NFMS prepared with high-purity synthetic slag containing varying Ca/Si and Mg/Ca levels. Previous work has established the synthetic procedure, reaction kinetics, pore structure, and compressive strength of these synthetic slags and their activation system [27]. This work is the extension of the previous work and aims to identify the degradation mechanisms of AA-NFMS exposed to $MgSO_4$ solution for up to 6 months using advanced characterization techniques to study changes in microstructure and phase assemblage. The degradation of AA-NFMS in $MgSO_4$ was evaluated by the mass change and compressive strength change. The study provides a comprehensive analysis of the behavior of AA-NFMS in $MgSO_4$ solutions, enhancing our understanding of this material and its potential applications. This research is crucial for advancing the practical use of AA-NFMS in sulfate rich environments.

2. Material and methods

2.1 Alkali-activated material synthesis

Four slags were synthesized with the composition of FeO-SiO_2-Al_2O_3-CaO-(MgO) using an Indutherm furnace, which were water-quenched to achieve a high amorphous content [28]. The synthesis procedure for these slags can be found in previous studies [25, 27]. The chemical compositions of the synthetic slags are listed in Table 1. After water-quenching, the slags were subsequently milled to a similar Blaine specific surface area (4000 ± 200 cm^2/g) using an attritor mill. Three of the slag samples, C_6A_1, C_3A_1, and C_2A_1, were designed to investigate the effect of Ca concentration on the sulfate resistance of AA-NFMS, while keeping the same Fe/Si and Al/Si ratio. The fourth slag, $C_2A_1M_2$, was prepared by replacing 4 wt% of CaO in C_3A_1 with MgO to evaluate the effect of Mg. C_2A_1 and $C_2A_1M_2$ have the same Ca content. Quantitative mineralogical analysis using XRD revealed that all the slag samples had more than 95% amorphous content. The detailed phase assemblage is given in Table A1.

Table 1 Chemical composition from XRF in mol% (any deviation from 100% is due to rounding errors)

	FeO	SiO_2	CaO	Al_2O_3	MgO	Formula of slag	Al_2O_3/SiO_2	Ca/Si	(Ca+Mg)/Si
C_6A_1	41	35	19	5	0	$F_{1.2}SC_{0.6}A_{0.1}$	0.1	0.6	0.6
C_3A_1	45	38	12	5	0	$F_{1.2}SC_{0.3}A_{0.1}$	0.1	0.3	0.3

C_2A_1	48	39	8	5	0	$F_{1.2}SC_{0.2}A_{0.1}$	0.1	0.2	0.2
$C_2A_1M_2$	44	37	8	5	7	$F_{1.2}SC_{0.2}A_{0.1}M_{0.2}$	0.1	0.2	0.4

The activation of NFMS was carried out using a solution of sodium silicate ($Na_2O{\cdot}1.65SiO_2$ with 65 wt. % water), which was prepared by mixing distilled water, sodium hydroxide pellets (>99 wt%, Sigma-Aldrich), and sodium silicate solution with molar ratio SiO_2/Na_2O=3.3 and 63.5 wt% H_2O (Silmaco). The activating solution was left to stand for at least one day to homogenize before use.

Mortar specimens of AA-NFMS were prepared in accordance with EN 196-1, with dimensions of 20 mm x 20 mm x 80 mm instead of the standard 40 mm x 40 mm x 160 mm due to the limited availability of synthetic slag. The mixture was prepared by mixing the slag, activator solution, and standard sand at a mass ratio of sand to slag of 3 and a mass ratio of liquid solution to slag of 0.5. CEM I 52.5 (PC) mortar was used as a reference to compare the macroscopic mass and compressive strength changes. The PC mortar was produced and cured in the same manner as the AA-NFMS. The composition of PC is detailed in Table 2. The materials proportion for paste and mortar samples is detailed in Table 3.

Table 2 Chemical composition of PC (in wt %)

Oxides	Fe_2O_3	SiO_2	CaO	Al_2O_3	MgO	SO_3	K_2O	Na_2O	Other [a]
wt %	3	20	63	5	2	3	0.6	0.3	3

[a] includes TiO_2, P_2O_3, Mn_2O_3 and LOI .

Table 3 Material proportion for paste and mortar samples (normalized to 100 g slag) (g)

	NFMS	Activator solution	Sand
Paste	100	40	/
Mortar	100	50	300

Additionally, AA-NFMS paste samples were prepared by mixing the slag and activator using a hand mixer for 3 minutes at an activator-to-slag mass ratio of 0.4 and then casting the mixture into a cylindrical mold with a diameter of 1.3 cm and height of about 3 cm. After casting, both mortar and

paste specimens were cured at room temperature for 28 days in a humidity chamber (20 ± 2 °C, and 40 ± 10 % humidity).

2.2 Experiment design

The present study aimed to investigate the macroscopic and microscopic damage of AA-NFMS when exposed to $MgSO_4$ solution.

To examine the microstructural changes induced by sulfate attack, paste samples after 28-day curing were embedded in a low-density epoxy. After the epoxy fully hardened, the bottom surface of the resin was ground away. Subsequently, the embedded samples were fully immersed and suspended in a 5 wt.% $MgSO_4$ solution, with only the bottom surface of AA-NFMS exposed to the $MgSO_4$ solution. The $MgSO_4$ solution was replaced every month for a total duration of 6 months. Subsequently, the embedded paste for each mix design was taken out from solution, and two cross-sections were cut from the middle of the sample along the longitudinal axes. The cross-sections were then stabilized by embedding them in low-density epoxy resin and polished, platinum-coated (2nm), and subsequently processed for scanning electron microscopy (SEM) and electron probe microanalysis (EPMA).

To enable an investigation of the final reaction products after the sulfate attack, a direct accelerated method was employed on powder AA-NFMS. This involved manually grinding the 28-day paste samples into powder, passing through a 100 µm sieve, and subsequently immersing approximately 5 g of paste powder from each mix design in 50 g of either $MgSO_4$ solution or water as a reference for 10 days. After immersion, the powder was filtered, and the reaction was stopped using a solvent exchange procedure [29] by rinsing with isopropanol two times and with diethylether one time, and then stored in a desiccator for X-ray diffraction (XRD) and Fourier-transform infrared spectroscopy (FTIR) measurement.

To assess the macroscopic damage, mortar samples of AA-NFMS and PC were fully immersed in either 5 wt.% $MgSO_4$ solution or water as a reference for up to 6 months. The mass changes of the samples were measured monthly and calculated as mentioned in [30, 31], and the compressive strength was measured at 1, 2, 4, and 6 months in triplicate. Prior to the measurements, the samples were taken out of the tank and dried with laboratory paper towels.

The experimental design for the study is depicted in Figure 1 Experiment process.

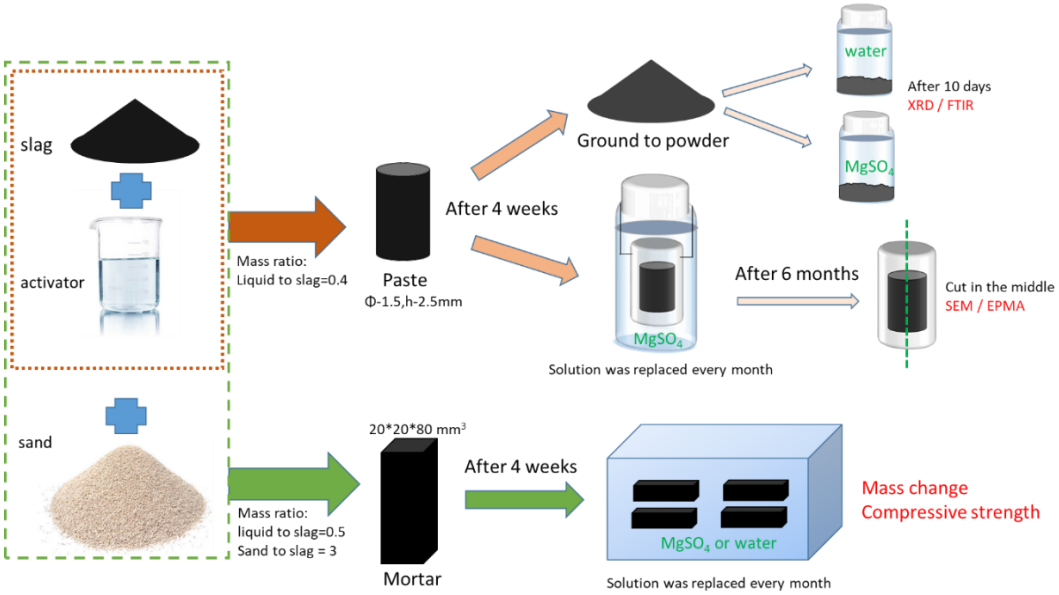

Figure 1 Experiment process of this work

2.3 Characterization

The compressive strength testing of the studied AA-NFMS or PC was carried out in accordance with the European standard EN 196-1, using an Instron 5985 testing machine with a 250 kN load cell at a displacement rate of 2 mm/min. The compressive strength change and mass change of the AAMs were calculated using the following equation:

$$\text{Compressive strength / mass change (\%)}=\left(\frac{A-B}{B}\right)\times 100\% \qquad \text{Eq. 1}$$

Here, A is the average compressive strength or mass of the samples immersed in $MgSO_4$ solution, and B is the average compressive strength of the samples immersed in water at the same exposure time or the mass of AA-NFMS before $MgSO_4$ exposure.

To assess the microstructural changes induced by sulfate attack, SEM and EPMA were employed. SEM observations were conducted using a Philips XL30 instrument operating at 10 kV with a working distance of 11 mm to obtain the morphology of the deterioration front. The elemental network mode mapping of Fe, Al, Ca, Si, Mg, Na, and S for the deterioration front was processed using JXA-8530F (JEOL) EPMA-WDS at 15 kV and 50 nA, with a dwelling time of 20 ms and a step size of 3 μm. Different standards were employed for EPMA analysis across various elements: Al and Si were assessed using almandine garnet ($Fe_3Al_2Si_3O_{12}$), Mg was quantified using olivine ($(Mg, Fe)_2SiO_4$), Na and Ca

were determined using plagioclase ((Na,Ca)Al(Al, Si)Si_2O_8), S was calibrated with galena (PbS), and the Fe content was measured utilizing hematite (Fe_2O_3). The EPMA maps of the corroded front were thresholded according to BSE level to separate pores, reacted binder, and unreacted slag. For AA-C_3A_1, an issue with the contrast only allowed a clear distinction between slag from the reacted binder and pores. For this sample, a second step was done to separate points with strong influence from pores by removing the measurement points with Si content < 10 wt.%. For comparative purposes, the data for each sample were shifted to start from the surface which was taken as the maximum of the Mg values indicating the center of $Mg(OH)_2$ layer covering the contact surface of the samples.

XRD was used to analyze the mineral composition of the samples. The powder obtained after 10 days of exposure to sulfate solution or water was measured using a D2 Phaser diffractometer (Bruker), with Cu Kα radiation (k = 1.54178 Å) of 30 kV and 10 mA. The patterns were recorded in a 2θ range of 10 -70°, with a 2°/min rate.

ATR-FTIR spectroscopy was employed to investigate the bonds between atoms of the powdered samples. A Bruker Alpha-P instrument was used to acquire the spectra within the 4000 - 400 cm^{-1} range at a resolution of 4 cm^{-1} and 32 scans per measurement. The spectra were obtained and processed using OPUS software.

Results and discussion

3.1 Microstructure of cylinder paste after sulfate attack for 6 months

To gain a conceptual understanding of the overall performance of the AA-NFMS in the presence of $MgSO_4$ solution, we focused on examining the microstructure of one of the samples subjected to a 6-month exposure to $MgSO_4$. The findings from the microstructural analysis of the embedded paste samples for AA-C_2A_1 are presented in Figure 2. The image provides a detailed view of the transition zone (in orange rectangle) and the corroded area (in green rectangle). It is important to note that some cracks were observed in the microstructure, which could have resulted from drying shrinkage, sample cutting, or the vacuum process involved in SEM sample preparation. The analysis revealed that there was no severe corrosion caused by the $MgSO_4$ solution as the total corrosion depth is less than 1 mm after 6 months exposure. Near the corroded front, there was an altered binder region exhibiting a higher

concentration of unreacted slag (in purple rectangle in Figure 2). This observation is likely linked to the dissolution of the reacted binder, as previously reported by Ye et al. [21].

To investigate the composition and elemental distribution in the studied area, EPMA analysis was performed, and the results are presented in Figure 3. In the corroded front, the structure is enriched in Mg and S. In the transition zone, a high concentration of Mg was noticed, indicating the presence of $Mg(OH)_2$. S can only be detected above this layer and did not penetrate the transition zone nor the binder. It is noteworthy that in the altered binder a significant amount of Ca has released from the inner AA-C_2A_1 to the solution, indicating the leaching of Ca ions during the experimental process. In the corded front, there are observable Ca-rich spots, likely resulting from carbonation and the formation of $CaCO_3$ phase. On the other hand, no significant changes were observed for Al, Si, and Fe.

Comparing Figure 2 and Figure 3, it can be observed that after the attack of $MgSO_4$, a layer consisting of mainly $Mg(OH)_2$ with minor $MgSO_4$ at the corroded surface is formed. This is followed by another dense layer of $Mg(OH)_2$, which acts as a barrier and slows down further attack, thus the presence of S is primarily located outside of the dense $Mg(OH)_2$ layer. Previous research has reported the effectiveness of using $Mg(OH)_2$ as a protective barrier due to its low solubility, which reduces the diffusion of sulfate ions [32, 33]. These findings are consistent with the current study.

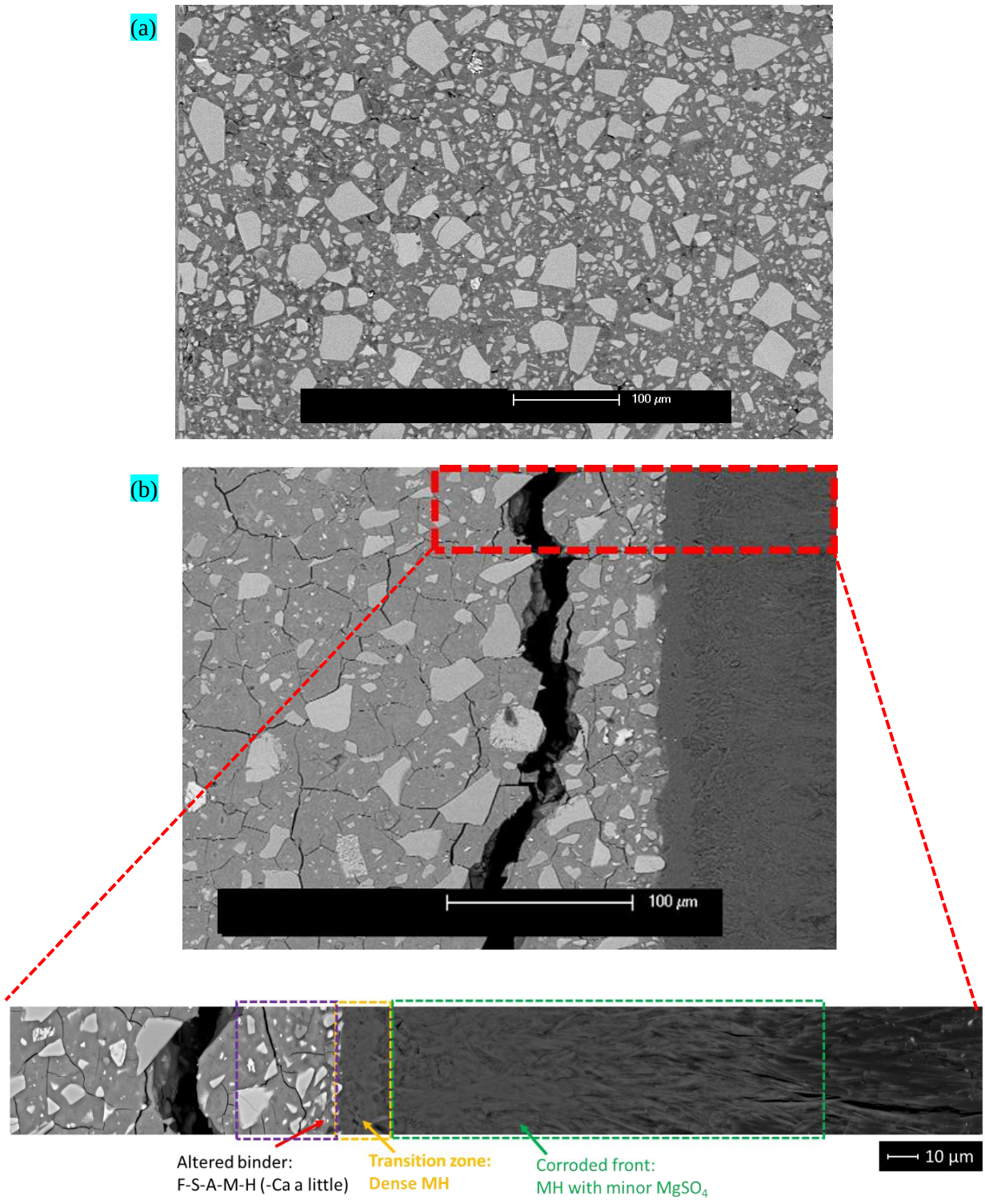

Figure 2 SEM image of AA-C_2A_1 (a) before $MgSO_4$ solution attack, and (b) after $MgSO_4$ solution attack for 6 months

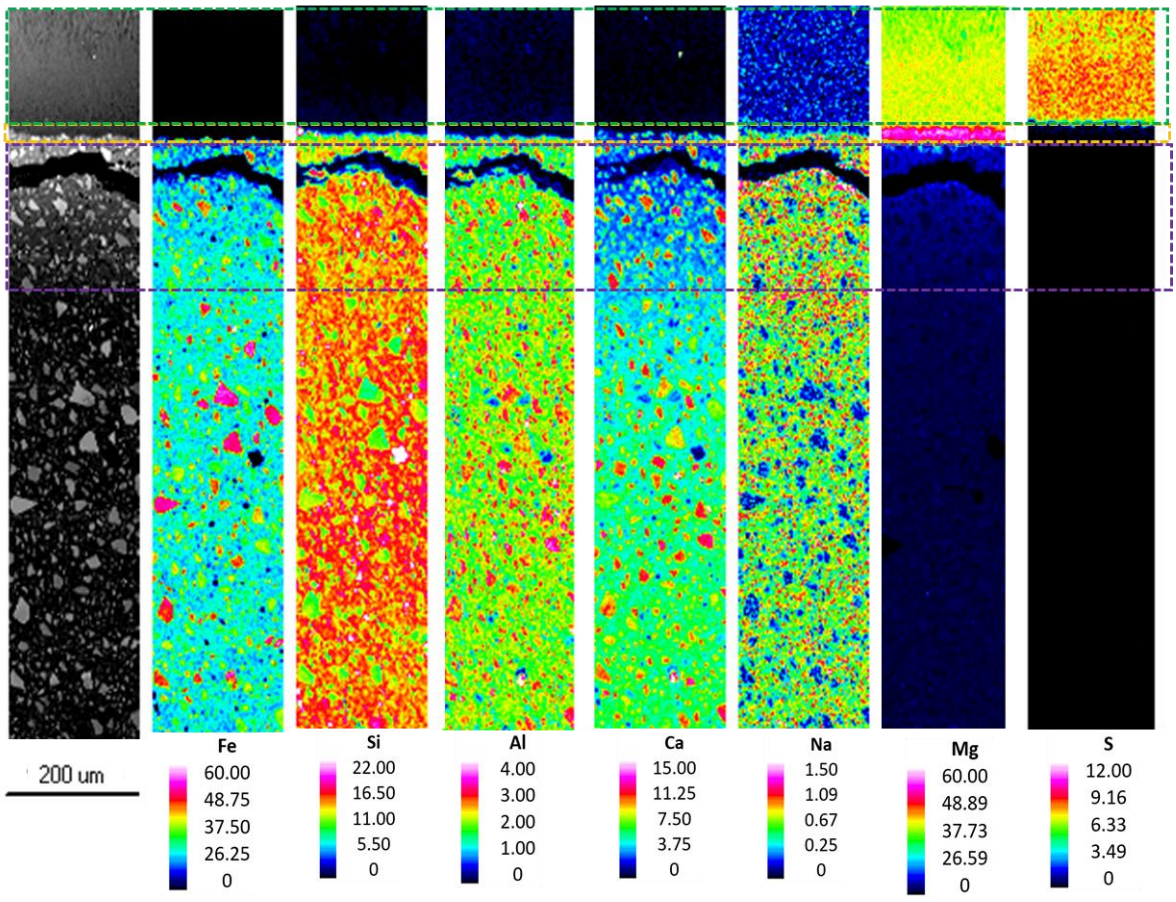

Figure 3 EPMA microchemical results of AA-C_2A_1 after $MgSO_4$ exposure

It is important to note that the measured composition from EPMA could be affected by the density and porosity of the intact and corroded area, the presence of H_2O, as well as the surface flatness. The corrosion front has higher porosity and a less flat surface due to sulfate attack, which might induce higher errors or standard deviations in the chemical composition measurement. Nevertheless, the hardened paste of AA-NFMS is composed of two solid constituents, namely unreacted slag and reacted binder. By separating the slag and the reacted binder through BSE-thresholding, the leaching of elements from these two components can be observed and more easily compared among samples. The original BSE images of the analyzed area for each AA-NFMS are shown in Figure 4 and the content of Ca in the binder as a function of depth is shown in Figure 5. Interestingly, despite the difference in Ca content of slags C_3A_1 and C_2A_1, they have a similar Ca content in the binder (Figure 5a). This similarity suggests that C_3A_1 and C_2A_1 may have a very similar binder. The Ca content in the binder (after $MgSO_4$ attack) is not linearly correlated to that in the slag. Yet, as the samples contain different amounts of Ca in the binder, additional information can be revealed by normalizing the Ca concentration to the average

content in the part of the binder assumed to be unaffected by leaching (Figure 5b), at a depth of 700-900 µm.

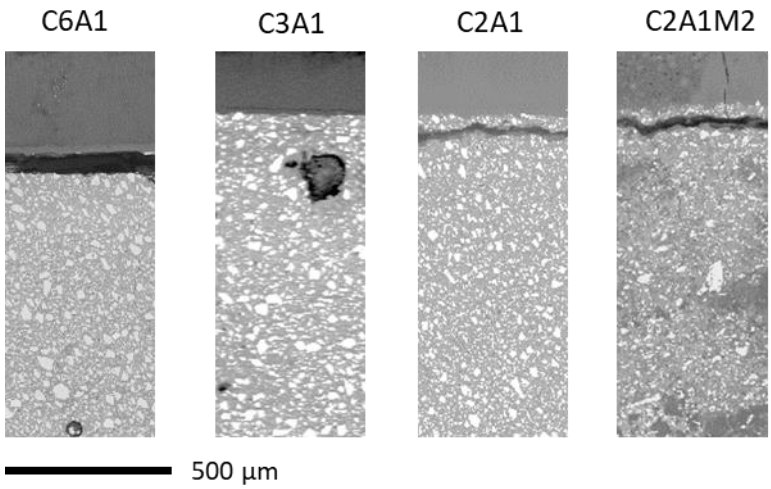

Figure 4 The BSE images of the EPMA mapping for each AA-NFMS

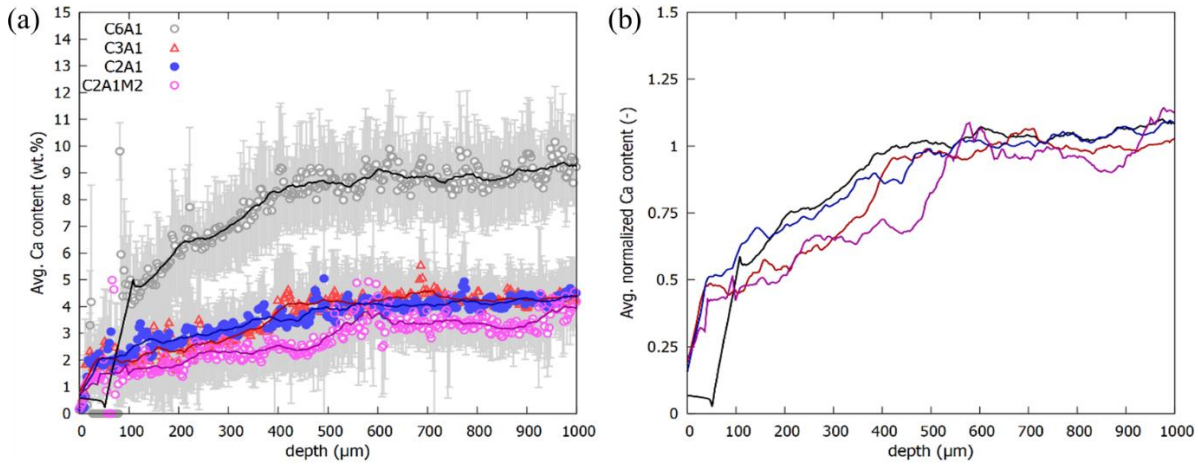

Figure 5 The average Ca content of the reacted binder part up to 1 mm from the surface before (a) and after normalization (b) to the value of the part of the binder that is assumed to be unaffected (700-900 µm). error bars indicate the standard deviation at each depth. The 19-point centered moving average (solid lines) are added as a guide for the eye.

As a result of the contact with the $MgSO_4$ solution, Ca in the binder is leached up to a depth of around 400-500 µm from the surface of all samples except AA-$C_2A_1M_2$, where the decreased Ca concentration is observed until a depth of 500-600 µm. The latter suggests the negative effect of replacing Ca with Mg on the $MgSO_4$ resistance of AA-NFMS. This can most likely be explained by the higher porosity, which was visually observed in this sample and supported by MIP results presented in [27], affecting the overall resistance of AA-$C_2A_1M_2$. Additionally, it may be influenced by a change in reacted phase assemblage. It is interesting to note that the fraction of Ca leached from the binder at the

surface is approximately the same for all samples, about 50 %. Despite the leaching of Ca from the binder, no decreased Ca concentration is observed in the slag (Figure 6) at any depth and thus all the slags can be considered inert with respect to leaching in the $MgSO_4$ solution.

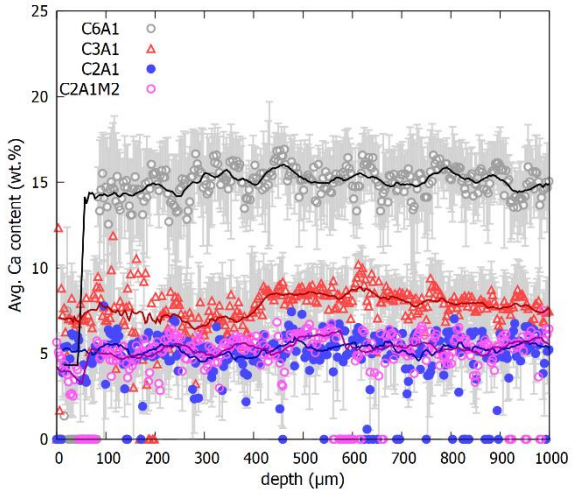

Figure 6 The average Ca content of the unreacted slag part up to 1 mm from the surface. error bars indicate the standard deviation at each depth. The 19-point centered moving average (solid lines) are added as a guide for the eye.

Al, Fe and Si appear to be more strongly resistant to leaching (Figure 7). For both Al and Si, no clear leaching effects are present (Figure 7a, c). In the case of Fe (Figure 7b), a slight decrease could be observed in the first 100 µm after the crack. However, it is not clear enough whether the effect is caused by leaching or measurement inaccuracies near the crack. Note that the strong pit in the curve for AA-C_3A_1 around a depth of 200 µm is most likely due to the large pore present at this point combined with the inaccurate thresholding of this pore due to a contrast issue in the measurement. The stability in the leaching of Al, Fe, and Si, occurring very close to the surface and to a limited extent, suggests that binders rich in these elements are more likely to have better resistance to $MgSO_4$. The restricted extraction of Fe is particularly noteworthy, and this limitation may contribute to the high sulfate salt resistance observed in Fe-rich AA-NFMS systems.

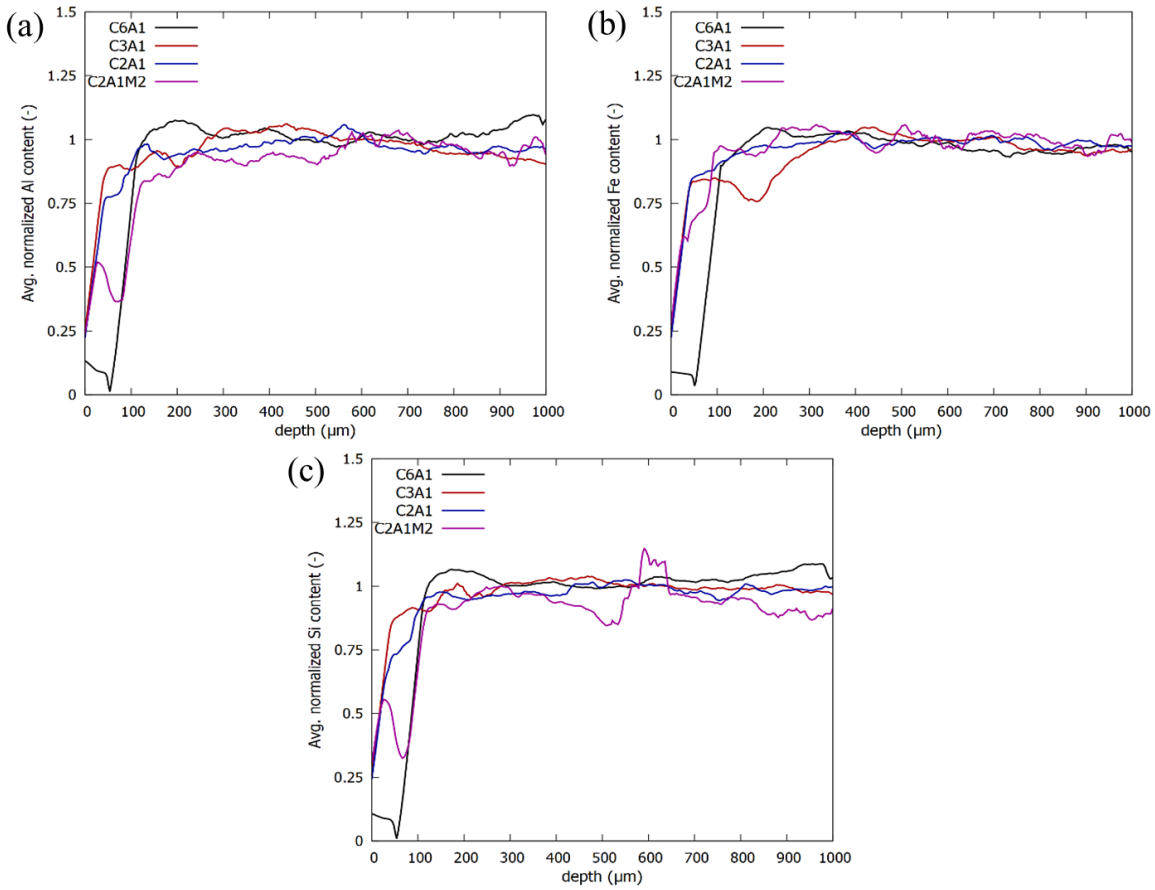

Figure 7 The 19-point centered moving average of the average Al (a), Fe (b) and Si (c) content of the binder part up to 1 mm from the surface before after normalization to the value of the part of the binder that is assumed to be unaffected (700-900 µm).

In general, the initiation of $MgSO_4$ attack occurs through the transfer of Mg^{2+} (and SO_4^{2-}) into the matrix [21], accompanied by the outward transport of Ca^{2+} and OH^- to the sulfate solution. The Mg^{2+} and OH^- react and form thin layers of $Mg(OH)_2$, which restrict the transport of SO_4^{2-} into the matrix. In Ca-rich systems like cement, the interaction of sulfate with Ca^{2+} occurs as long as the concentrations of Ca^{2+}, Al^{3+}, and SO_4^{2-} in the pore solution allow it, as these will control the SO_4^{2-} concentration and transport via their equilibrium with ettringite and AFm phases [7]. Once Ca^{2+} and Al^{3+} are depleted, sulfate can penetrate to greater depths. The precipitation of gypsum further depletes Ca^{2+} from the main reaction product, leading to the degradation of the main structure. However, the unique characteristics of AA-NFMS, including its low Ca content and high Fe content, lead to a restrained release of elements from the binding phases when exposed to $MgSO_4$, especially when compared to calcium-rich systems. Furthermore, while a dense layer of $Mg(OH)_2$ forms, providing additional corrosion protection –a phenomenon similar to other cementitious materials like cement –the inhibitory effect of $Mg(OH)_2$ in

AA-NFMS surpasses that of cement. This is evidenced by the absence of SO_4^{2-} migration into the AA-NFMS matrix and no subsequent obvious gypsum formation, in contrast to cement where abundant gypsum is still evidently present [34]. The disparity in the structure of the $Mg(OH)_2$ layer between AA-NFMS and cement is not yet understood, underscoring the need for focused research to uncover the underlying factors behind this variation. Nevertheless, these findings here suggest that the AA-NFMS system holds promise as a sustainable alternative to cement in sulfate-rich environments.

3.2 Microstructure of powder paste after sulfate attack for ten days

To investigate the final reaction products of AA-NFMS after $MgSO_4$ exposure in a high concentration, powdered samples were studied. The procedure involved curing AA-NFMS paste for 28 days, followed by grinding the material into powder form, which was then directly subjected to $MgSO_4$ solution for 10 days. This approach accelerates the reaction significantly, facilitated by the increased contact area. As in the hardened cylinders, there is a $Mg(OH)_2$ layer blocking the interaction between $MgSO_4$ solution and AA-NFMS. In these samples, focus can be put solely on the chemical interaction of the reacted binder and slag with $MgSO_4$, assuming $MgSO_4$ can infiltrate the pore solution of AA-NFMS, disregarding transport properties. Thus, it is essential to acknowledge that this method does not mirror the real-world response of sizable monoliths or structures, but is used as a tool to study the final reaction products.

The microstructure of AA-C_6A_1 powder after exposure to $MgSO_4$ solution for 10 days is depicted in Figure 8, and an element mapping from EPMA is shown in Figure 9. In the reacted binder of the powder samples, regions abundant in Mg and O are evident. This signifies the presence of $Mg(OH)_2$, similar to what is observed in hardened cylinder paste samples. However, a notable difference was observed when comparing it to the microstructure of hardened cylindrical paste samples that were exposed to $MgSO_4$ solution for 6 months. In the case of the cylinders, a protective layer composed of $Mg(OH)_2$ developed, serving as an effective barrier against the diffusion of ions. This layer significantly limited the formation of gypsum. In contrast, in the microstructure of AA-C_6A_1 powder after $MgSO_4$ attack, gypsum was observed abundantly.

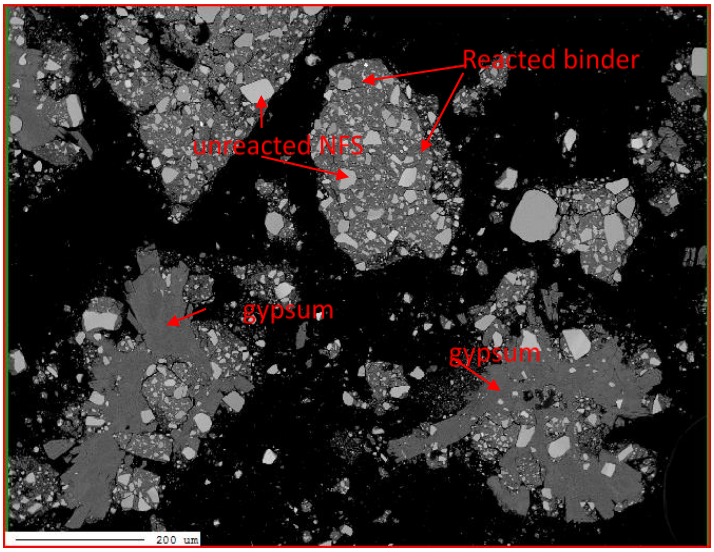

Figure 8 Microstructure of powder AA-C_6A_1 after 10 days in $MgSO_4$ solution

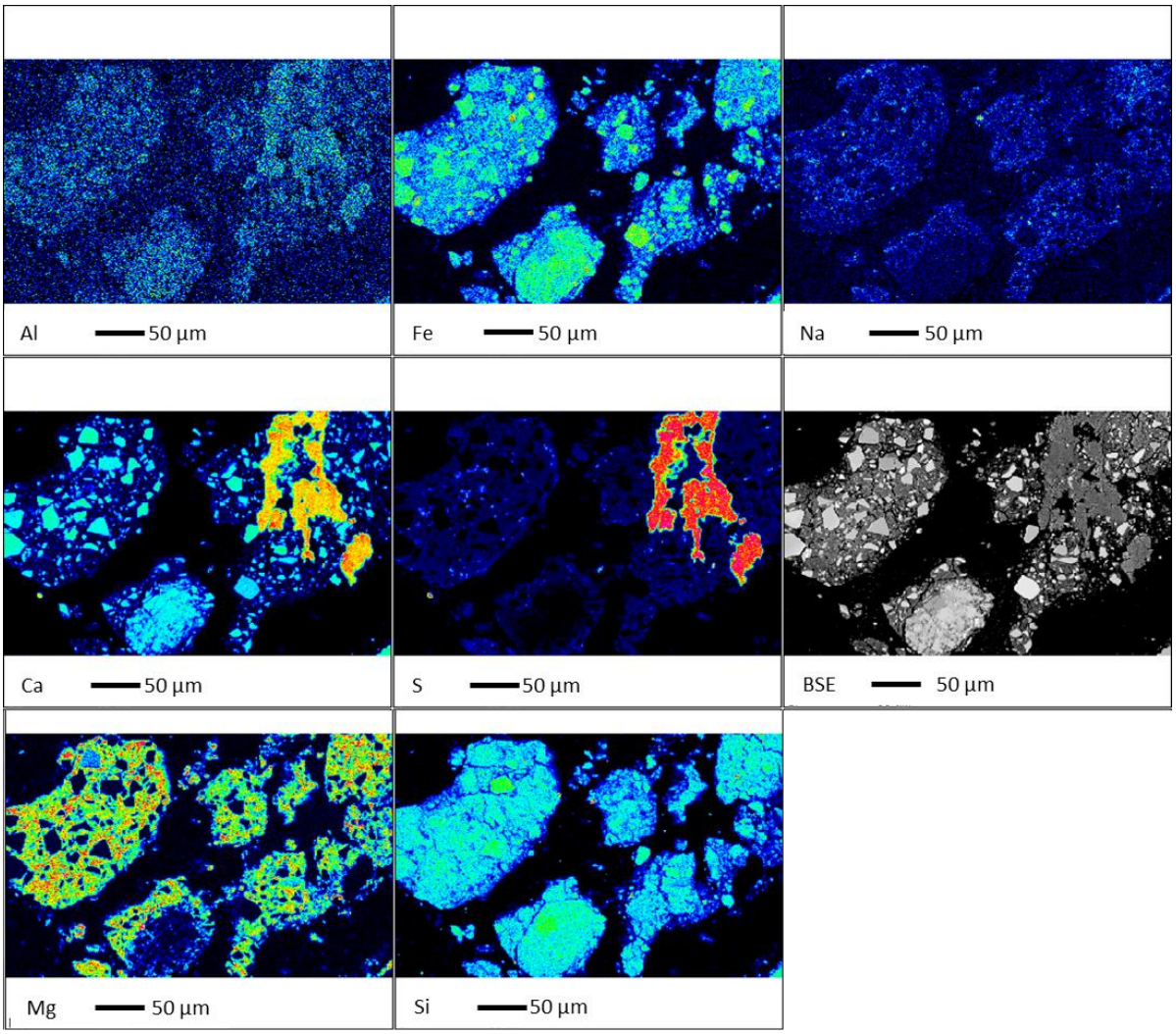

Figure 9 Element mapping of powder AA-C_6A_1 after 10 days in $MgSO_4$ solution

This difference can be attributed to several underlying factors. The exposure time may have an influence, as the powder was exposed to the sulfate solution for 10 days, while the hardened cylinder was exposed for 6 months. When considering powder samples, the significantly enlarged surface area boosts reaction, and the high availability of sulfate ions accelerates the reaction kinetics. In this context, Ca^{2+}, being highly mobile ions within the system, readily engages in the rapid and substantial formation of gypsum. While the study of powder samples could lay the groundwork for understanding mechanisms, given the slow $MgSO_4$ attack on hardened monolith cylinders, direct interpreting behaviors may not be exact. The degradation mechanism observed in powder samples suggests the potential for gypsum formation in AA-NFMS after $MgSO_4$ exposure. However, due to the presence of a $Mg(OH)_2$ layer in the monolith cylinder, gypsum does not form in the AA-NFMS matrix. Therefore, it becomes apparent that, in addition to chemical degradation mechanisms associated with sulfate attack on AA-NFMS, the transport properties of the pastes also determine the degradation mechanism caused by $MgSO_4$ exposure.

3.3 XRD analysis

The XRD patterns of AA-NFMS paste in both water and $MgSO_4$ are presented in Figure 10. The XRD patterns of AA-NFMS after 10 days of exposure to water reveal a prominent hump and minor peaks of cristobalite (COD 9009686) and olivine (COD 9000469). The presence of minor cristobalite may be attributed to slag contamination during the milling or grinding process prior to exposure to the $MgSO_4$ solution.

Analyzing the XRD patterns of samples exposed to both water and $MgSO_4$ highlights certain phase transformations triggered by the influence of $MgSO_4$ exposure. In the case of AA-NFMS in $MgSO_4$, the hump and crystalline peaks of cristobalite and olivine remain unchanged, while new phases of gypsum (COD 9015350) are observed due to the leaching of Ca^{2+} from AA-NFMS to the $MgSO_4$ solution. Peaks for $Mg(OH)_2$ are not detected, which may be attributed to its limited quantity or small grain size with low crystallinity. $MgSO_4$ attack on Portland cement leads to substantial decalcification and the formation of M-S-H [33]. However, in this study, the similarity of the Fe^{2+}-containing

phyllosilicate-like amorphous structure of the AA-NFMS to M-S-H poses challenges in confirming the presence of M-S-H. The M-S-H as described by Bernard et al. [35], in which the magnesium is arranged trioctahedrally in brucite-like layers, is completely analogous to the trioctahedral Fe^{2+}-layers in the AA-NFMS described by Peys et al. [36]. The amorphous phase likely pertains to a structure in which the magnesium is partially taking place at the position of Fe, while Ca – also suggested to be potentially present in the trioctahedral layers – is leached from the system. In addition, comparing AA-C_6A_1, C_3A_1 and C_2A_1, it is seen that there is more gypsum forming as the Ca content in the system increases. However, when comparing AA-C_2A_1 and AA-$C_2A_1M_2$, possessing similar Ca content, a greater gypsum formation is observed in AA-$C_2A_1M_2$. This observation might suggest that the reacted binder in AA-$C_2A_1M_2$ is weaker compared to that in AA-C_2A_1 when exposed to $MgSO_4$ solution. This finding may give another explanation for the higher decalcification depth observed in EPMA for AA-$C_2A_1M_2$ compared to AA-C_3A_1 and AA-C_2A_1, as shown in Figure 5b, where the decalcification depth for AA-C_3A_1 and C_2A_1 is approximately 400-500 µm, whereas for AA-$C_2A_1M_2$, it is around 500-600 µm.

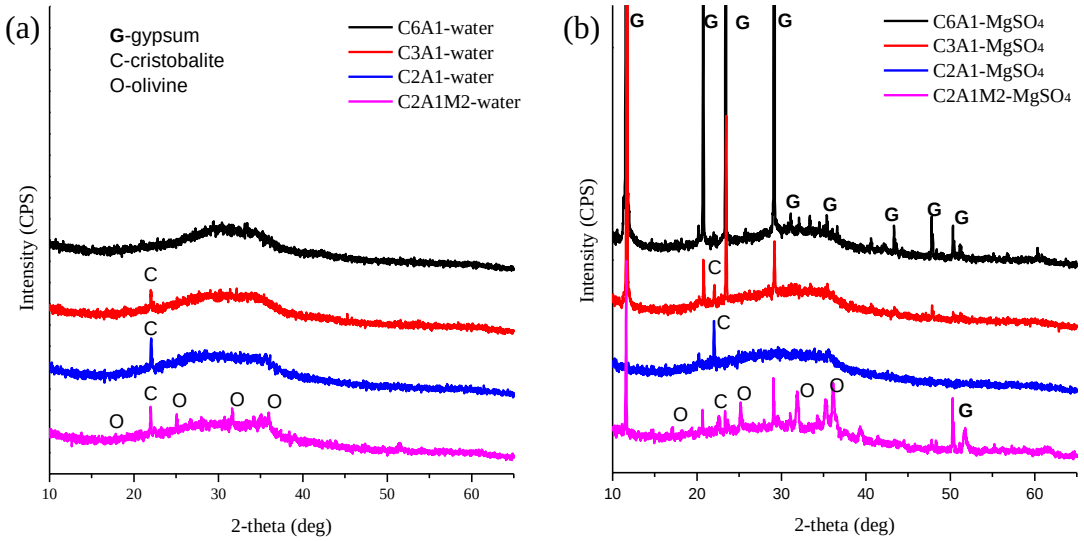

Figure 10 XRD of paste in water and in MgSO4 (a)in water (b)in MgSO4

3.4 FTIR analysis

The FTIR analysis in the region between 400 and 1200 cm^{-1}, as depicted in Figure 11, reveals important information about the polymerization of the main binder phases C-M-(N-)F-A-S-H gel. For

AA-NFMS cured in water, the prominent band observed at approximately 965-986 cm^{-1} corresponds to Si-O-T stretching vibrations (T = Si, Al, or Fe).

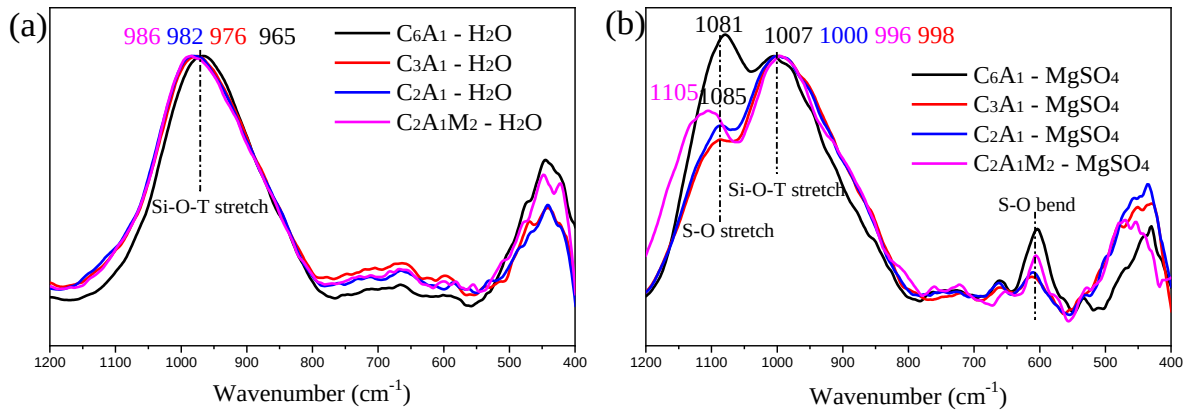

Figure 11 FTIR of AA-NFMS in (a) in water; (b) in $MgSO_4$ solution

After exposure to $MgSO_4$, the Si-O-T stretching band undergoes a shift to a higher wavenumber, which may be attributed to the leaching of network modifiers (Ca, Mg, and/or Fe) from the binder, as detected in the aforementioned EPMA or XRD analysis. This shift becomes more pronounced with an increasing Ca/Si ratio, suggesting a higher degree of degradation associated with elevated Ca/Si ratios [37]. In all AA-NFMS samples, the main band is situated around 1000 cm^{-1} after exposure to $MgSO_4$ solution. The results suggest that the diverse Ca/Si ratios in the studied cases have a limited effect on the extent of polymerization of the final reaction product of AA-NFMS after $MgSO_4$ attack. Additionally, the emergence of new bands around 1100 and 610 cm^{-1} indicates the formation of gypsum, which is also observed in study [30], consistent with the earlier XRD results mentioned earlier. However, it is noteworthy that the SO_4^{2-} band for AA-$C_2A_1M_2$, which contains Mg in NFMS, is observed at a higher wavenumber compared to that without Mg in the AA-NFMS system, indicating a distinct S-O environment. This discrepancy suggests a change in sulfate products during the $MgSO_4$ attack, though the reason for this remains unclear. Further investigation is necessary in this area.

3.5 Mass change and compressive strength change

Figure 12 displays the mass change of mortar specimens following exposure time. The PC had the highest mass gain compared to all AA-NFMS samples. Among the AA-NFMS, C_6A_1 showed the highest mass gain, followed by C_3A_1, $C_2A_1M_2$, and C_2A_1. Increasing the Ca concentration in the AA-

NFMS system resulted in a higher mass gain. Plotting the mass change as a function of CaO content in the slag revealed a clear linear correlation between CaO content and mass change, suggesting that the mass gain is predominantly attributed to gypsum formation. Notably, for C_6A_1 with 16% CaO, there was a significant mass gain after four months, indicating considerable gypsum formation in AA-C_6A_1 when exposed to $MgSO_4$.

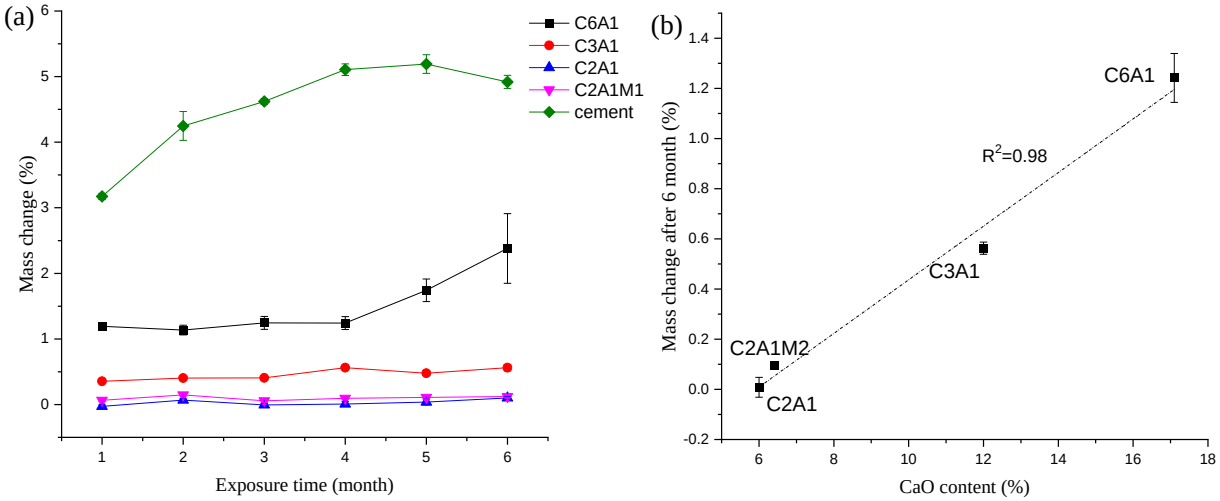

Figure 12 Mass change for mortar specimens exposed to 5 % MgSO4 solution. Note: Due to the abrupt increase in mass change observed in AA-C6A1 after 4 months, during which the samples experienced significant degradation, the mass change used in the fitted Figure 9(b) was based on the 4-month period rather than the originally intended 6-month duration.

The compressive strength of mortar specimens over different exposure periods is illustrated in Figure 13. When immersed in water (Figure 13a), the compressive strength of all mix designs increased during the 6-month duration. Among the AA-NFMS variants, C_6A_1-AAM exhibited the highest strength, indicating the significant contribution of Ca to compressive strength, which aligns with previous studies [23, 25, 38]. No clear effect of Mg replacement for Ca on the long-term compressive strength was observed. However, when subjected to $MgSO_4$ solution, the strength development pattern changed noticeably. Both cement and AA-C_6A_1 specimens experienced a significant decrease in strength. The strength of the medium CaO system (AA-C_3A_1) and low CaO systems (AA-C_2A_1, AA-$C_2A_1M_2$) remained relatively stable, with some fluctuations attributed to the combined effects of strength increase in the undamaged binder region and strength decrease in the corroded outer region and also the variation among samples. It is important to note that after 6 months of exposure to $MgSO_4$ solution, the final strength of Portland cement was similar to that of AA-C_3A_1. In terms of strength changes, Portland

cement exhibited a substantial reduction throughout the entire exposure period. C_6A_1-AAM also experienced severe degradation, particularly after 4 months, which corresponds with the observed mass change. Compared to specimens stored in water, Portland cement samples and AA-C_6A_1 experienced approximately 40% and 50% strength reduction, respectively, after 6 months of exposure to $MgSO_4$ solution. Both AA-C_2A_1 and AA-$C_2A_1M_2$ experienced a strength loss of approximately 20% by the end of the exposure period. On the other hand, AA-C_3A_1, with a medium CaO content of approximately 10 wt% in the slag, exhibited the lowest strength reduction of 10%. The findings from FTIR (more pronounced shift of the main Si-O-T band of higher Ca/Si in Figure 11) suggest that a higher Ca/Si ratio corresponds to increased degradation after $MgSO_4$ exposure. Conversely, the reference samples cured in water reveal that an elevated Ca/Si ratio leads to higher mechanical strength. Therefore, the equilibrium between weaker corroded areas and stronger intact areas, associated with the increasing Ca/Si ratio, could play a role in the medium Ca/Si ratio yielding the lower reduction of the strength.

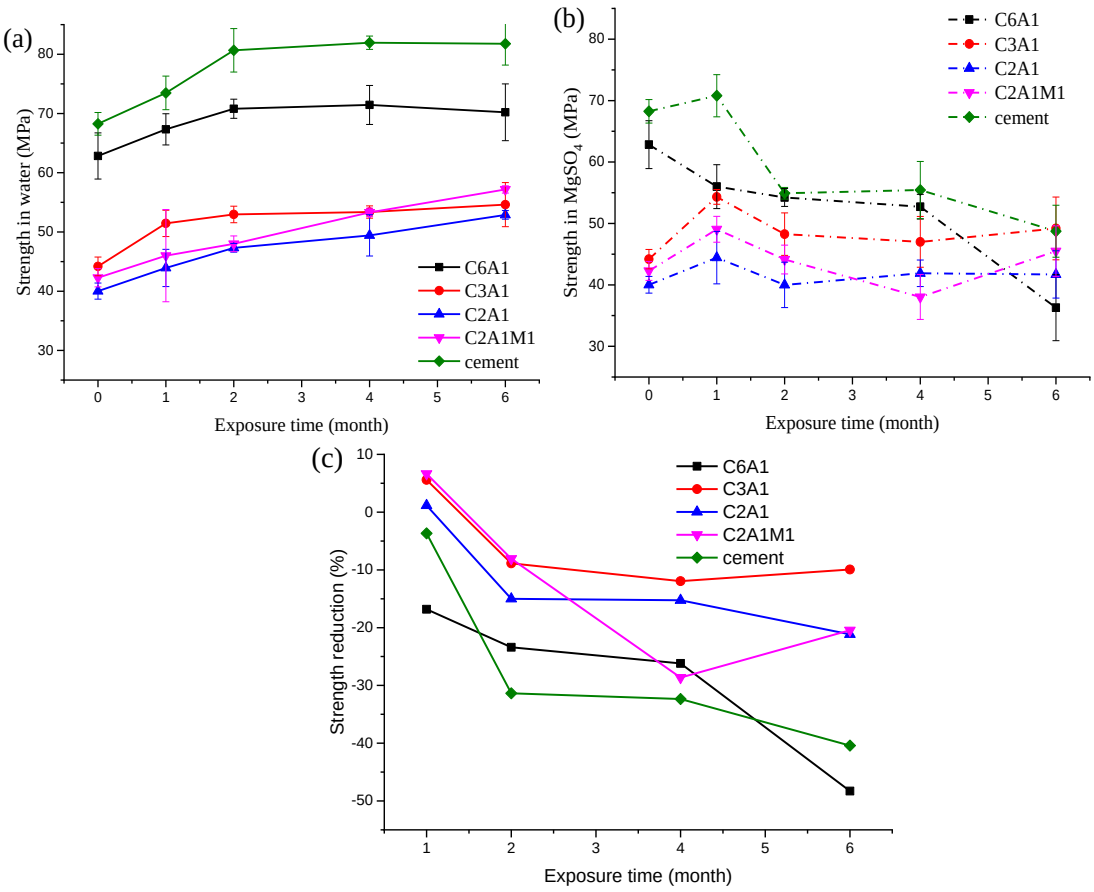

Figure 5 Compressive strength (change) for mortar specimens exposed to 5 % $MgSO_4$ solution

3.6 Degradation mechanisms

This study aimed to elucidate the degradation mechanism of Fe-silicate AA-NFMS after exposure to $MgSO_4$ solution. The results indicate that the deterioration of AA-NFMS primarily occurs within the reacted binder, as the unreacted slag remains inert in terms of leaching in the $MgSO_4$ solution. Upon exposure to the $MgSO_4$ solution, the leached OH^- from AA-NFMS matrix reacts with Mg^{2+} in the solution, forming a dense layer of $Mg(OH)_2$. This layer acts as a barrier, preventing SO_4^{2-} in the $MgSO_4$ solution from migrating into AA-NFMS, and thus inhibits the formation of gypsum. This mechanism differs from that in cement, where SO_4^{2-} migrates into the structure, leading to the formation of expansive gypsum and severe decalcification, which contributes to the degradation of cement [16, 39]. Among the primary elements in AA-NFMS (Ca, Fe, Si, and Al), Ca is the most mobile and readily leaches out from the AA-NFMS matrix, and the leaching of Al, Fe, and Si occurs very close to the surface and to a limited extent. Despite $MgSO_4$ exposure, AA-NFMS retains a decent compressive strength, particularly AA-C_3A_1 with a strength of 50 MPa after 6 months of exposure to $MgSO_4$ solution, which experiences only around 10% reduction in strength compared to samples cured in water. The medium and low-Ca system (AA-C_3A_1 and AA-C_2A_1) undergoes limited structural change. This provides an opportunity for low Ca system of AA-C_2A_1. Despite AA-C_2A_1 exhibiting lower mechanical performance, it is still suitable for applications where high strength is not crucial, such as coating materials, due to its stability in $MgSO_4$ solution. The promising strength of AA-NFMS after $MgSO_4$ exposure is due to the reaction product of AA-NFMS that is relatively Ca-poor and Fe-rich, compared to conventional Ca-silicate cementitious materials, as well as due to the formation of a dense $Mg(OH)_2$ layer. The schematic representation of the degradation process is depicted in Figure 14.

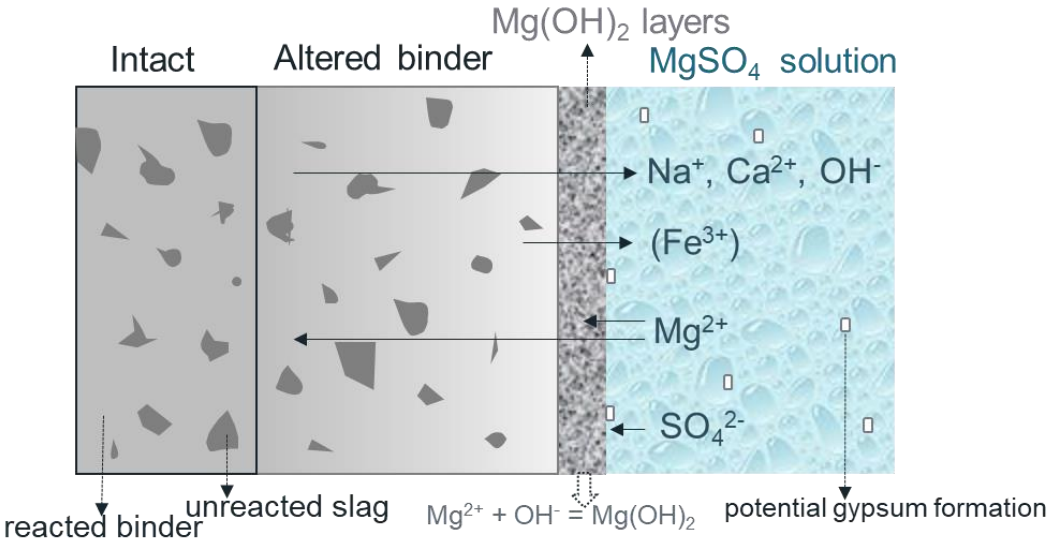

Figure 6 Schematic diagram of deterioration mechanism of AA-NFMS in $MgSO_4$ solution

Conclusion

The objective of this study was to explore the degradation mechanism of alkali-activated Fe-rich non-ferrous metallurgical slag (AA-NFMS) when exposed to 5 wt.% $MgSO_4$ for 6 months. Additionally, this study aimed to examine the influence of NFMS chemistry on the degradation process. The results demonstrated that AA-NFMS with an appropriate chemistry exhibited superior resistance to $MgSO_4$ compared to Portland cement, as evidenced by the mass change and compressive strength results. Four different types of AA-NFMS, varying in Ca/Si and Mg/Ca ratios, were examined. The depth and extent of decalcification were similar across different Ca/Si ratios and originated from the reacted binder (around 50% Ca was still present in the reacted binder compared to the levels before exposure to $MgSO_4$). Conversely, when Ca was partially replaced by Mg, there was a higher decalcification depth, resulting in reduced resistance to $MgSO_4$ attack. This may be attributed to the elevated porosity observed or weaker reacted binder after the replacement of Ca with Mg. Notably, samples with middle-level Ca concentrations (around 10% in NFMS) exhibited more favorable properties, as they obtained higher compressive strength with the lowest strength reduction after exposure to $MgSO_4$ for 6 months.

The excellent durability of AA-NFMS against $MgSO_4$ attack can be attributed to several factors. Firstly, the low Ca content in AA-NFMS minimized the exchange with Mg when exposed to $MgSO_4$

solution. Secondly, the high Fe content with a structural role in the phase assemblage of AA-NFMS, compared to conventional construction materials, rendered it relatively stable during exposure to $MgSO_4$, resulting in low dissolution. Lastly, the formation of a $Mg(OH)_2$ layer acted as a protective barrier, effectively retarding further corrosion.

In summary, this study provided valuable insights into the performance and degradation behavior of AA-NFMS materials when subjected to sulfate attack. The findings serve as a foundation for future research endeavors aimed at optimizing the composition, understanding the underlying mechanisms, and developing strategies to enhance the durability and sustainability of AA-NFMS-based constructions in sulfate-rich environments.

Declaration of competing interest

The authors declare that they do not have any competing financial interests or personal relationships that might be perceived as influencing the findings presented in this paper.

Author contribution

Nana Wen – Conceptualization, data curation, formal analysis, investigation, methodology, visualization, writing -original draft; Vincent Hallet – Formal analysis, methodology, supervision, writing – review and editing; Arne Peys – Supervision, writing – review and editing; Yiannis Pontikes – Funding acquisition, resources, supervision, writing – review and editing.

Reference

[1] G. Habert, S.A. Miller, V.M. John, J.L. Provis, A. Favier, A. Horvath, K.L. Scrivener, Environmental impacts and decarbonization strategies in the cement and concrete industries, Nature Reviews Earth & Environment 1(11) (2020) 559-573.
[2] J.L. Provis, S.A. Bernal, Z. Zhang, The Decarbonization of Construction—How Can Alkali-Activated Materials Contribute?, Engineering (2023).
[3] K.L. Scrivener, R.J. Kirkpatrick, Innovation in use and research on cementitious material, Cement and Concrete Research 38(2) (2008) 128-136.
[4] A. Peys, V. Isteri, J. Yliniemi, A.S. Yorkshire, P.N. Lemougna, C. Utton, J.L. Provis, R. Snellings, T. Hanein, Sustainable iron-rich cements: Raw material sources and binder types, Cement and Concrete Research 157 (2022) 106834.
[5] J.L. Provis, A. Palomo, C. Shi, Advances in understanding alkali-activated materials, Cement and Concrete Research 78 (2015) 110-125.
[6] V. Ponomar, J. Yliniemi, E. Adesanya, K. Ohenoja, M. Illikainen, An overview of the utilisation of Fe-rich residues in alkali-activated binders: Mechanical properties and state of iron, Journal of Cleaner Production 330 (2022).
[7] R. Ragoug, O.O. Metalssi, F. Barberon, J.-M. Torrenti, N. Roussel, L. Divet, J.-B. d'Espinose de Lacaillerie, Durability of cement pastes exposed to external sulfate attack and leaching: Physical and chemical aspects, Cement and Concrete Research 116 (2019) 134-145.
[8] S. Afridi, M.A. Sikandar, M. Waseem, H. Nasir, A. Naseer, Chemical durability of superabsorbent polymer (SAP) based geopolymer mortars (GPMs), Construction and Building Materials 217 (2019) 530-542.
[9] F. Mittermayr, M. Rezvani, A. Baldermann, S. Hainer, P. Breitenbücher, J. Juhart, C.-A. Graubner, T. Proske, Sulfate resistance of cement-reduced eco-friendly concretes, Cement and Concrete Composites 55 (2015) 364-373.
[10] M. Santhanam, M.D. Cohen, J. Olek, Effects of gypsum formation on the performance of cement mortars during external sulfate attack, Cement and Concrete Research 33(3) (2003) 325-332.
[11] P.K. Mehta, Mechanism of sulfate attack on portland cement concrete — Another look, Cement and Concrete Research 13(3) (1983) 401-406.
[12] F.P. Glasser, J. Marchand, E. Samson, Durability of concrete — Degradation phenomena involving detrimental chemical reactions, Cement and Concrete Research 38(2) (2008) 226-246.
[13] A. Baldermann, M. Rezvani, T. Proske, C. Grengg, F. Steindl, M. Sakoparnig, C. Baldermann, I. Galan, F. Emmerich, F. Mittermayr, Effect of very high limestone content and quality on the sulfate resistance of blended cements, Construction and Building Materials 188 (2018) 1065-1076.
[14] U.H. Jakobsen, K. De Weerdt, M.R. Geiker, Elemental zonation in marine concrete, Cement and Concrete Research 85 (2016) 12-27.
[15] K. Sotiriadis, M. Hlobil, A. Viani, P. Mácová, M. Vopálenský, Physical-chemical-mechanical quantitative assessment of the microstructural evolution in Portland-limestone cement pastes exposed to magnesium sulfate attack at low temperature, Cement and Concrete Research 149 (2021).
[16] J. Marchand, I. Odler, J. Skalny, Sulfate Attack on Concrete, (2001).
[17] Q. Yuan, Z. Liu, K. Zheng, C. Ma, Chapter 2 - Inorganic cementing materials, in: Q. Yuan, Z. Liu, K. Zheng, C. Ma (Eds.), Civil Engineering Materials, Elsevier2021, pp. 17-57.
[18] Z. Baščarević, M. Komljenović, Z. Miladinović, V. Nikolić, N. Marjanović, R. Petrović, Impact of sodium sulfate solution on mechanical properties and structure of fly ash based geopolymers, Materials and Structures 48(3) (2014) 683-697.
[19] M.O. Yusuf, Performance of slag blended alkaline activated palm oil fuel ash mortar in sulfate environments, Construction and Building Materials 98 (2015) 417-424.
[20] A. Allahvedi, H. Hashemi, Investigating the resistance of alkali-activated slag mortar exposed to MgSO4, International Journal of Civil Engineering 13 (2015) 379-387.

[21] H. Ye, Z. Chen, L. Huang, Mechanism of sulfate attack on alkali-activated slag: The role of activator composition, Cement and Concrete Research 125 (2019).
[22] T. Bakharev, Durability of geopolymer materials in sodium and magnesium sulfate solutions, Cement and Concrete Research 35(6) (2005) 1233-1246.
[23] C. Siakati, A.P. Douvalis, V. Hallet, A. Peys, Y. Pontikes, Influence of CaO/FeO ratio on the formation mechanism and properties of alkali-activated Fe-rich slags, Cement and Concrete Research 146 (2021).
[24] C. Siakati, R. Macchieraldo, B. Kirchner, F. Tielens, A. Peys, D. Seveno, Y. Pontikes, Unraveling the nano-structure of a glassy CaO-FeO-SiO2 slag by molecular dynamics simulations, Journal of Non-Crystalline Solids 528 (2020).
[25] J. Van De Sande, A. Peys, T. Hertel, H. Rahier, Y. Pontikes, Upcycling of non-ferrous metallurgy slags: Identifying the most reactive slag for inorganic polymer construction materials, Resources, Conservation and Recycling 154 (2020) 104627.
[26] I. Garcia-Lodeiro, E. Aparicio-Rebollo, A. Fernández-Jimenez, A. Palomo, Effect of calcium on the alkaline activation of aluminosilicate glass, Ceramics International 42(6) (2016) 7697-7707.
[27] N. Wen, A. Peys, T. Hertel, Y. Pontikes, Impact of Ca, Al, and Mg on Reaction Kinetics, Pore Structure, and Performance of Fe‐rich Alkali‐activated Slag, Journal of the American Ceramic Society (2024).
[28] C. Siakati, A.P. Douvalis, P. Ziogas, A. Peys, Y. Pontikes, Impact of the solidification path of FeO_x–SiO_2 slags on the resultant inorganic polymers, Journal of the American Ceramic Society 103(3) (2019) 2173-2184.
[29] A. Machner, M. Zajac, M. Ben Haha, K.O. Kjellsen, M.R. Geiker, K. De Weerdt, Limitations of the hydrotalcite formation in Portland composite cement pastes containing dolomite and metakaolin, Cement and Concrete Research 105 (2018) 1-17.
[30] M. Nasir, M.A. Megat Johari, M. Maslehuddin, M. Olalekan Yusuf, Magnesium sulfate resistance of alkali/slag activated silico-manganese fume-based composites, Construction and Building Materials 265 (2020) 120851.
[31] M. Nasir, M.A.M. Johari, M. Maslehuddin, M.O. Yusuf, Sodium sulfate resistance of alkali/slag activated silico–manganese fume-based composites, Structural Concrete 22(S1) (2021) E415-E429.
[32] M. Santhanam, M. Cohen, J. Olek, Differentiating seawater and groundwater sulfate attack in Portland cement mortars, Cement and Concrete Research 36(12) (2006) 2132-2137.
[33] S.R. Pinto, C. Angulski da Luz, G.S. Munhoz, R.A. Medeiros-Junior, Durability of phosphogypsum-based supersulfated cement mortar against external attack by sodium and magnesium sulfate, Cement and Concrete Research 136 (2020) 106172.
[34] D. Bonen, M.D. Cohen, Magnesium sulfate attack on portland cement paste-I. Microstructural analysis, Cement and Concrete Research 22(1) (1992) 169-180.
[35] E. Bernard, B. Lothenbach, C. Chlique, M. Wyrzykowski, A. Dauzères, I. Pochard, C. Cau-dit-Coumes, Characterization of Magnesium Silicate Hydrate (M-S-H), Cement and Concrete Research (2019).
[36] A. Peys, C.E. White, H. Rahier, B. Blanpain, Y. Pontikes, Alkali-activation of CaO-FeOx-SiO2 slag: Formation mechanism from in-situ X-ray total scattering, Cement and Concrete Research 122 (2019) 179-188.
[37] T.A. Aiken, J. Kwasny, W. Sha, Resistance of fly ash geopolymer binders to organic acids, Materials and Structures 53(5) (2020) 115.
[38] C. Siakati, A.P. Douvalis, A. Peys, Y. Pontikes, Binary, ternary and quaternary Fe-rich slags: Influence of Fe and Si substitution by Ca and Al on the atomic structure and reactivity, Conference: 6th International Slag Valorisation Symposium (2019).
[39] Y.-K. Cho, J.H. Kim, S. Jung, Y. Chung, Y. Jeong, Importance of Cation Species During Sulfate Resistance Tests for Alkali-Activated FA/GGBFS Blended Mortars, Materials (2019).

Appendix

Table A.1 Phase assemblage of the synthetic slag, in wt%

	Amorphous	Olivine	Cristobalite
C6A1	>98		
C3A1	>98		
C2A1	>98		
C2A1M2	95	4	1

Quantificative XRD was carried out with the software Topas Academic